OPEN

NPG Asia Materials (2016) 8, e291; doi:10.1038/am.2016.92
www.nature.com/am

ORIGINAL ARTICLE

In situ TEM study of deformation-induced crystalline-to-amorphous transition in silicon

Yue-Cun Wang[1], Wei Zhang[1], Li-Yuan Wang[2], Zhuo Zhuang[2], En Ma[1,3], Ju Li[1,4] and Zhi-Wei Shan[1]

The mechanism responsible for deformation-induced crystalline-to-amorphous transition (CAT) in silicon is still under considerable debate, owing to the absence of direct experimental evidence. Here we have devised a novel core/shell configuration to impose confinement on the sample to circumvent early cracking during uniaxial compression of submicron-sized Si pillars. This has enabled large plastic deformation and *in situ* monitoring of the CAT process inside a transmission electron microscope. We demonstrate that diamond cubic Si transforms into amorphous silicon through slip-mediated generation and storage of stacking faults (SFs), without involving any intermediate crystalline phases. By employing density functional theory simulations, we find that energetically unfavorable single-layer SFs create very strong antibonding interactions, which trigger the subsequent structural rearrangements. Our findings thus resolve the interrelationship between plastic deformation and amorphization in silicon, and shed light on the mechanism underlying deformation-induced CAT in general.
NPG Asia Materials (2016) **8,** e291; doi:10.1038/am.2016.92; published online 22 July 2016

INTRODUCTION

The crystalline and amorphous phases are the two principal states of silicon, and the transformation[1–6] between them has attracted great attention. One route to realize the crystalline-to-amorphous transition (CAT) in Si is mechanical loading. This has relevance in practical applications; for example, an amorphous layer always forms after mechanical polishing of single crystalline Si (c-Si) wafers, causing damage that degrades the performance of integrated circuits and electronic devices.[7,8] The CAT has also been recognized to have a role in the incipient plasticity of bulk c-Si at room temperature.[7,9,10] Stress-induced CAT in Si has in fact been widely observed under various mechanical loading conditions, such as indentation,[6,10–15] ball milling,[16,17] scratching[2,7] and bending.[18,19] Clarke *et al.*[6] firstly reported straining-induced amorphous Si (a-Si) through indentation experiments. On the basis of the sharp drop in the electric resistance measured during the loading process, they speculated that a possible path for the CAT is the transition from an intermediated high-pressure crystalline phase (β-tin) to a-Si upon rapid unloading. We refer the diamond cubic Si as Si-I phase and the β-tin Si as Si-II phase. This viewpoint was further strengthened by the discontinuous load-depth curves obtained in indentation tests.[11,15] Subsequently, Si-II phase is frequently cited as a transition state for the CAT of Si. However, a-Si was also reported to exhibit sharp resistance change under pressure,[20] and discontinuous load-depth curves may be caused by processes other than phase transformation, for example, massive dislocation nucleation and motion and so on.[10] As such, in the absence of direct evidence, the necessity of the Si-II phase during the CAT process is uncertain, and has in fact been challenged by several research groups.[13,14,21] In an effort to directly observe the response of c-Si to indentation, Minor *et al.*[22] carried out indentation tests inside TEM. They found no phase transformation and only dislocation-mediated metal-like plastic deformation. The work by Ge *et al.*[12] suggested that confinement is necessary for CAT in c-Si, and this was later confirmed by Chrobak *et al.*[10] The appropriate constrains on c-Si, for one thing, may improve the stress level in it. Theoretical calculation predicted that the critical von Mises stress to induce CAT in Si is ~9.7 GPa ($(9/2)^{1/2}\times$ the maximum octahedral shear stress of 4.6 GPa).[9] This magnitude can be reached easily in indentation tests. However, under indentation, the samples are usually in a complex stress state with high strain gradients, complicating subsequent quantitative analysis. Uniaxial loading, in comparison, can greatly simplify the stress condition. But the c-Si samples, even at submicron size, will fracture in a brittle manner well before the loading stress can reach the critical level needed for CAT.[23] Therefore, another crucial role of the confinement should be to suppress the premature brittle cracking in c-Si. In the following, we report the design of a novel core/shell sample configuration that applies confinement on the electron transparent samples, which enabled real-time visualization of deformation-induced CAT of c-Si under uniaxial compression inside TEM, as well as *in situ* monitoring of the

[1]Center for Advancing Materials Performance from the Nanoscale (CAMP-Nano) & Hysitron Applied Research Center in China (HARCC), State Key Laboratory for Mechanical Behavior of Materials, Xi'an Jiaotong University, Xi'an, PR China; [2]Applied Mechanics Lab, School of Aerospace Engineering, Tsinghua University, Beijing, PR China; [3]Department of Materials Science and Engineering, Johns Hopkins University, Baltimore, MD, USA and [4]Department of Nuclear Science and Engineering and Department of Materials Science and Engineering, Massachusetts Institute of Technology, Cambridge, MA, USA
Correspondence: Professor W Zhang or Professor Z-W Shan, Center for Advancing Materials Performance from the Nanoscale (CAMP-Nano) & Hysitron Applied Research Center in China (HARCC), State Key Laboratory for Mechanical Behavior of Materials, Xi'an Jiaotong University, West Xianning Road 28, Xi'an, Shaanxi 710049, PR China.
E-mail: wzhang0@mail.xjtu.edu.cn or zwshan@mail.xjtu.edu.cn
Received 25 February 2016; revised 20 April 2016; accepted 5 May 2016

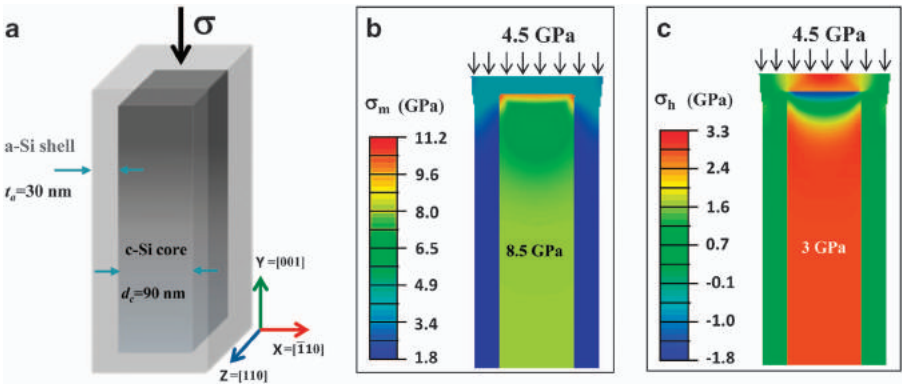

Figure 1 Core/shell sample and stress distribution in it. (**a**) Schematic illustration of the core-/shell-structured pillar, with the thickness of the a-Si shell, $t_a = 30$ nm, and effective diameter of the c-Si core, $d_c = 90$ nm. The black arrow indicates the compression-loading in the $00\bar{1}$ direction. (**b–c**) The colored nephograms show the von Mises stress σ_m and hydrostatic stress σ_h distributions on the $Z = 1/2$ plane of the pillar from the finite element method calculation. The 4.5 GPa applied stress is the measured average yield stress. The σ_m in the c-Si core is raised markedly to ~8.5 GPa, and the corresponding σ_h is ~3 GPa.

defect accumulation mechanism responsible for the amorphization. We also use *ab initio* simulations to reveal the atomistic and energetics details underlying the observed amorphization upon storage of defects in the c-Si.

MATERIALS AND METHODS

Sample preparation

Boron-doped <100>-oriented single crystal Si wedge (2 μm wedge width) was chosen as the starting material. The Si wedge was initially designed to facilitate the nanoparticles compression in TEM, and more details of the Si wedge can be found in reference.[24] All the core-/shell-structured Si samples in this work were fabricated via a Helios NanoLab 600 dual-beam FIB system (FEI, Hillsboro, OR, USA) under 30 kV accelerating voltage with the beam current of Ga ions sequentially decreasing from 440 pA (coarse cutting) to 1.5 pA (fine polishing). To minimize the taper, we fabricated pillars with square cross-section via glancing cutting on the lateral surface and tilting the stage by 1.2° to compensate for the conical-shape ion beam profile upon the final thinning of both sides of the pillar. As shown in Supplementary Figure S5a, the taper angle for the as-fabricated pillar is quite small and can be ignored. Prior to mechanical loading, we took the scanning electron microscope images (Supplementary Figure S5b) for measuring the cross-section area. We also cross-checked the core-shell structures at the local scale using high-resolution TEM (HRTEM) (Supplementary Figure S9). In particular, the c-Si/a-Si interface looks rather smooth, which ensures that the a-Si shell adheres closely to the c-Si core during deformation.

Mechanical compression and TEM measurements

In situ compression test was conducted using a Hysitron PI 95 PicoIndenter (Hysitron, Minneapolis, MN, USA) (Supplementary Figure S4) inside a JEOL 2100F TEM (200 keV; JEOL, Tokyo, Japan). The diameter of the flat diamond punch was ~2 μm. The tests were all controlled under a fixed displacement rate of 2 nm s^{-1}. For all the samples, engineering stress was calculated through dividing load by cross-sectional area (A) that was measured from the scanning electron microscope image of the fabricated pillars, see Supplementary Figure S5b. The effective sample size d was taken to be $\sqrt{A}$. The engineering strain was defined to be the ratio of the deformation displacement of the pillar (that is, the displacement reading minus the contribution from the substrate) to its initial height (the distance between the top end and the substrate). The deformed samples were further thinned by using M1040 Nano Mill (Fischione, Bethlehem, PA, USA) for HRTEM observation. One side of each sample was milled at the 15° tilt angle (the Ar ion beam to specimen surface) for 30 min, and the other side was thinned at −10° tilt angle for 40 min by 1 kV Ar^+.

Finite element method calculation

We used a three-dimensional finite element model (Figure 1a) to calculate the stress distribution in the core/shell structures through the commercially available software ABAQUS 6.13 (SIMULIA, Dassault, Paris, France). An eight-node linear brick, reduced integration element was used with the element size about 5 nm, consisting about 80 000 elements. The displacement in the Y-direction is constrained to the bottom surface $Y = 0$; the Z-direction displacement was constrained on the $(X = 0, Y = 0, Z = 0)$ node; the X-direction displacement was constrained on the $(X = 0, Y = 0, Z = 150$ nm) node. The quasi-static displacement loading was used and all the calculations were made when the applied nominal external stress reached 4.5 GPa. The elastic modulus of a-Si shell (ideal elastoplastic body) and c-Si core (ideal elastic body) are assigned to be 33 and 130 GPa, respectively. The yield stress of a-Si shell and c-Si core are 4.0 and 7.6 GPa, respectively.[23]

DFT simulations

We performed DFT simulations using the Vienna Ab initio simulation package (VASP) code,[25] employing gradient-corrected functionals[26] and projector augmented-wave potentials.[27] The atomic relaxation simulations were performed at 0 K on $8 \times 8 \times 2$ k-point grids[28] for the smaller Si models, and $2 \times 2 \times 2$ k-point grids for the larger Si model. The employed energy cutoff of the electron wavefunction is 300 eV. The convergence of the calculations with respect to the energy cutoff and kpoint mesh are demonstrated in Supplementary Table S1. The quantum chemistry bonding analyses were carried out using the Local Orbital Basis Suite Towards Electronic-Structure Reconstruction (LOBSTER) code,[29] which retrieves the wavefunction information from the VASP calculations. Both gradient-corrected functionals and modified Becke and Johnson potential[30] were employed for the bonding analysis, shown in Supplementary Figure S10. Modified Becke and Johnson potential is shown to be more accurate in simulating the energy band gap of Si. Both methods yield the same results.

RESULTS

Design of electron transparent samples with confinement

In a previous TEM study,[23] we found that the Si pillars fabricated with focused ion beam (FIB) under 30 kV accelerating voltage always exhibit a c-Si core/a-Si shell structure. The thickness of the amorphous outer shell is always ~30 nm regardless of the pillar diameter. Surprisingly, this Ga^+ bombardment-introduced a-Si exhibits stable plastic flow during uniaxial compression. The measured apparent elastic modulus is 30–40 GPa (Supplementary Figure S1), which is about a quarter of the value for the c-Si counterpart. A thorough investigation of the mechanical behavior of a-Si will be reported elsewhere. Inspired by these findings, we surmise that the FIB

fabricated shell may provide the desired confinement on c-Si core, for observing the CAT process inside a TEM.

We first carried out finite element method calculations (see details in the Materials and methods section) to examine the magnitude and distribution of the stresses in the core-/shell-structured Si pillars under global uniaxial compression loading. It was found that with the confining shell, the stress experienced by the c-Si core can be significantly higher than the nominal applied axial stress for samples with a diameter less than ~200 nm. A schematic illustration of one typical example is shown in Figure 1a. The effective diameter of the c-Si core and the thickness of the a-Si shell is $d_c = 90$ nm and $t_a = 30$ nm, respectively. Figure 1b and c show the von Mises (σ_m) and hydrostatic (σ_h) stress distributions on the $Z = 1/2$ plane of the pillar upon yielding. The nominal applied uniaxial compressive stress $\sigma = 4.5$ GPa is the measured average yield stress at which the pillar starts to deviate from the elastic behavior (Supplementary Figure S2). Note that at this point the σ_m in the c-Si core reaches as high as ~8.5 GPa (Figure 1b), which is close to the predicated critical value of 9.7 GPa for CAT in Si,[9] and the σ_h in the c-Si core is ~3 GPa. Compared with bare c-Si pillar (Supplementary Figure S3), the stress on the c-Si core is greatly raised, owing to the constraint imposed by the a-Si shell. As such, the CAT process would be expected to occur in the c-Si with this kind of core/shell sample.

Real-time CAT path in Si

Typical examples are shown in Figure 2. The c-Si core and a-Si shell can be easily distinguished from the TEM bright-/dark-field images (left inset in Figure 2a and b). The uniaxial compression experiments were carried out in TEM (see the *in situ* nanomechanical setup in Supplementary Figure S4) on two core-/shell-structured Si pillars with the same effective diameter $d = 152$ nm (Supplementary Figure S5). The almost overlapping engineering stress-strain curves (Figure 2a) indicate that the two samples experienced identical structural evolution. Both samples experienced extensive and very smooth plastic flow without cracking. As it is not feasible to catch both dark-field images and selected area diffraction patterns simultaneously in one sample, we recorded the real-space evolution in sample-1, and the reciprocal-space evolution in sample-2. The snapshots that correspond to global strain $\varepsilon = 0$, 12, 20 and 24% are shown in Figure 2b and c. The first selected area diffraction pattern indicated that the c-Si core before loading ($\varepsilon = 0\%$) was clearly a diamond cubic Si-I phase. Dislocation slip was observed after the onset of yielding, and the slip bands, marked by the orange dashed lines in Figure 2b, were oriented at an angle of ~54° with respect to the (001) surface, indicating that they were aligned on the {111} glide planes. These slip bands originated from the loading front and developed toward the undeformed region with increasing strain. The diffraction spots from the crossed slip band network were elongated, which stems from the high-density defects in this region (Figure 2b, $\varepsilon = 12\%$). As the compression proceeded further (for example, Figure 2b, $\varepsilon = 20\%$), the yellow-boxed region with heavy plastic deformation transformed to an amorphous phase, as evidenced by its diffraction pattern. Afterwards, the increasing plastic strain in the deformed part of the sample should mainly come from the plastic flow of this newly formed a-Si phase. The 'mushroom' shape of the compressed pillar ($\varepsilon = 24\%$) resembles the compressed pure a-Si pillar (Supplementary Figure S1), and their selected area diffraction patterns are also identical. The undeformed (bottom) part of the pillar still exhibits the crystalline-like contrast. Clearly, the CAT in c-Si is driven by plastic deformation. The *in situ* selected area diffraction patterns (and Supplementary Movie 1) unambiguously demonstrate that there were no other phase transformations, for example, Si-I → Si-II, during the entire loading and unloading process. Instead, crystalline Si-I directly transforms into a-Si, driven by slip-mediated plastic deformation. For more details see Supplementary Movie 1.

HRTEM characterization of the CAT process

The details in the CAT process were further elucidated via HRTEM characterization. Four core-/shell-structured Si pillars, similar to those discussed above, were fabricated and compressed to obtain different levels of plastic strain, $\varepsilon_p = 1$, 5, 18 and 25%. The corresponding engineering stress-strain curves are shown in Figure 3a. The compressed pillars were further thinned to ~100 nm in a NanoMill (Fischione) using low-energy Ar^+ for HRTEM experiments. We selected a typical region from each of the four compressed pillars

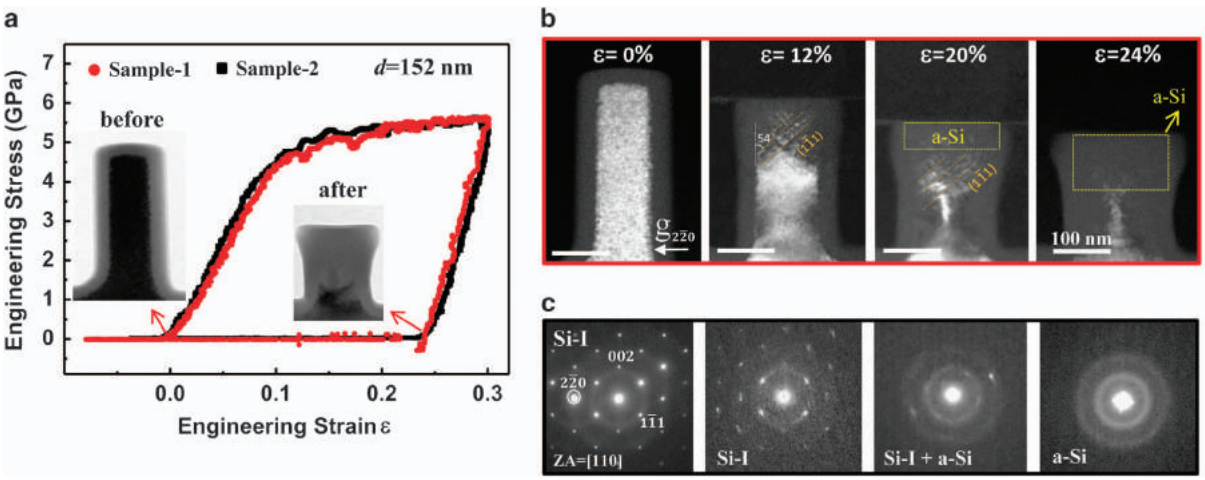

Figure 2 *In situ* observation of the CAT process during uniaxial compression recorded in the real and reciprocal space. (**a**) Engineering stress-strain curves of sample-1 (red) and sample-2 (black) with effective diameter $d \sim 152$ nm. The insets are the bright-field transmission electron microscope images of sample-1 before and after loading. (**b**) Extracted snapshots from the recorded movie showing the amorphization evolution with increasing engineering strain ε. The accumulation of slip bands along {111} planes (orange dashed lines) leads to amorphization at the deformation front. (**c**) Selected area electron diffraction patterns (SAEDPs) corresponding to (**b**) with the same ε. Note that there were no new spots of any other intermediate crystalline phases during the entire CAT process. a-Si, amorphous Si; CAT, crystalline-to-amorphous transition. ZA, zone axis.

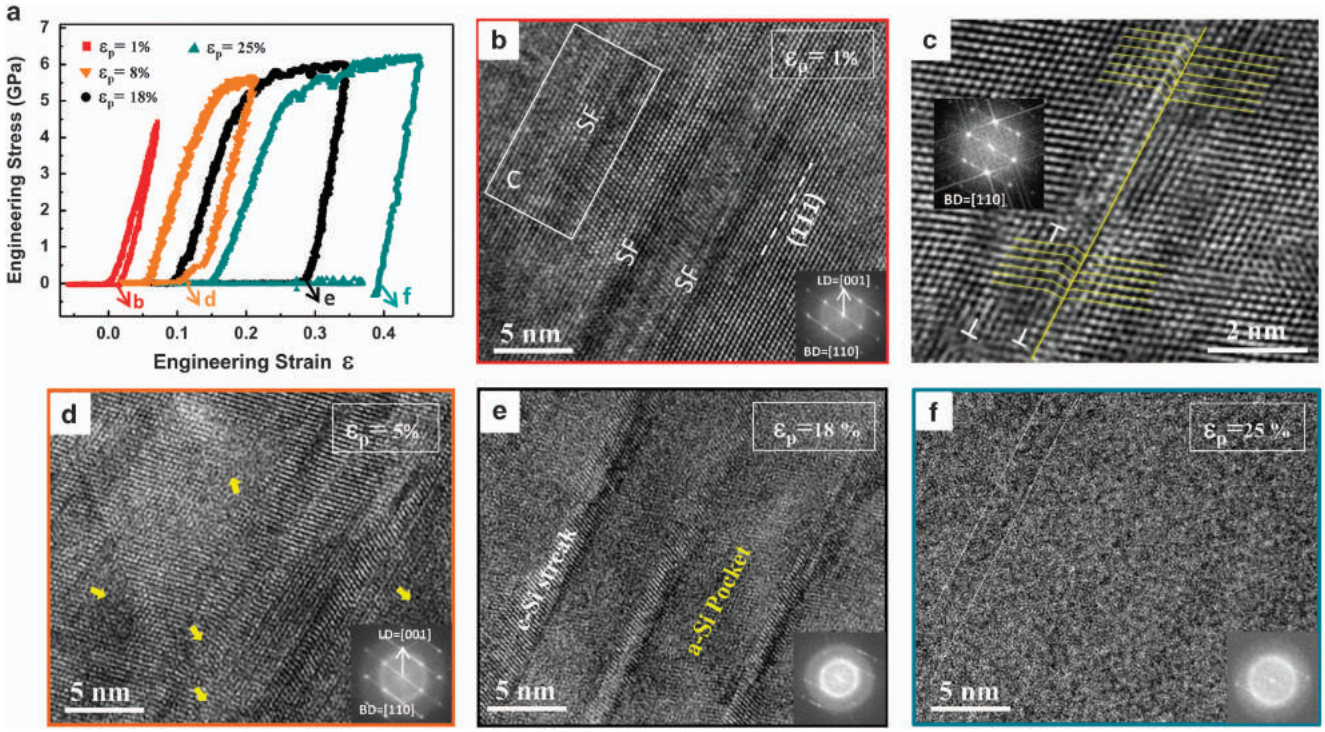

Figure 3 High-resolution transmission electron microscope characterization of the crystalline-to-amorphous transition process. (**a**) Engineering stress-strain curves of four core-/shell-structured Si pillars compressed to different deformation level ε_p. The loading direction (LD) is along [001], the axial direction of pillars. (**b**) Occurrence of many slip bands containing SFs upon plastic deformation ($\varepsilon_p = 1\%$). (**c**) The zoom-in image of the white-boxed region in (**b**) showing the detailed structure of the SF and the misfit dislocations around it. (**d**) Amorphization of the domains in or near the SFs (as marked by the yellow arrows). (**e**) Many directional 'amorphous pockets', separated by the c-Si ones. (**f**) The final amorphous packets in texture-like stripes, as indicated by the white dashed lines. The beam direction (BD) is [110]. a-Si, amorphous Si; c-Si, crystalline Si; SF, stacking faults.

and studied the structures in detail (see their global views in Supplementary Figure S6). Many slip bands appeared upon small plastic deformation (Figure 3b), and fast Fourier transform image (the inset) illustrates the existence of high-density defects along {111} planes in these bands. A zoom-in view clearly shows that the slip bands contain stacking faults (SFs) and dislocations (Figure 3c, indicated by the white box in Figure 3b). Therefore, the incipient plasticity was carried out by partial or full dislocations[31] rather than the CAT. The planar defects are presumably created by the high von Mises stress, and stored in the c-Si. As ε_p increased to 5%, some domains in or near the SFs became blurred in the HRTEM images (marked by the yellow arrows in Figure 3d), indicating the onset of amorphization. Upon further straining, these amorphous domains expanded and formed directional 'amorphous pockets' along the [111] direction, as shown in Figure 3e; ($\varepsilon_p = 18\%$). Some crystal streaks with clear Si-I structural feature still remained, and were separated in space by the 'amorphous pockets', resulting in many c-Si/a-Si interfaces. At the stage of $\varepsilon_p = 25\%$ (Figure 3f), almost all the crystalline parts got amorphized, as the expanding amorphous pockets expand to impinge on one another, eventually forming amorphous–amorphous interfaces (AAIs).[32] The resultant $[111]_{orig.\ crystal}$-inclined amorphous–amorphous interfaces are indicated by the white parallel dashed lines, which is an indicator of deformation induced CAT. During the whole CAT process, there are no other intermediate crystalline phases, demonstrating a direct phase transition from the original Si-I phase to the amorphous phase.

To recapitulate, we have demonstrated that under compression loading, a direct CAT takes place due to the accumulation of plastic strain and profuse SFs. The next step is to understand the deformation-induced CAT process at the atomic and electronic scale. To this end, DFT simulations are used next to gain further insight into the energetics and atomic-scale details of the SFs formation, storage and the ensuing amorphization.

DFT simulations of the CAT process at the atomic scale

In diamond cubic Si, the atomic planes follow the stacking pattern of -AABBCC- along the [111] direction, where A, B and C corresponds to the (0, 0), (1/3, 2/3) and (2/3, 1/3) positions of the (111) plane (see the parallelogram with the lattice parameter $a_{hex} = 3.84$ Å in Supplementary Figure S7). The Si model is also shown in Figure 4a, showing -AABBCCAABBCC- stacking. First, we model the pairwise stacking faults, giving -AABBAABBCCBB-, shown in Figure 4b, where a CC pair is removed, but a BB pair is added. The insertion or elimination of a pairwise layers are termed as intrinsic or extrinsic SF in Si.[33] The energy elevation is quite small, only ~6.4 meV/atom, in line with previous theoretical calculations.[33,34] The small energy difference can be understood from the bonding configuration, that is, the number of tetrahedral bonds per atom remains unchanged. By performing quantum chemistry bonding analysis using the crystal orbital overlap population (COOP)[29,35] method, we have quantified the bonding contributions (blue curves in Figure 4). The favorable bonding (positive values) and unfavorable antibonding (negative values) interactions between the two models differ only slightly, in particular near the Fermi level, E_F. This suggests that a high population of SFs can be present in c-Si without severe lattice distortions. Upon further mechanical deformation, more SFs are generated and accumulated, and the single-layer SFs (SSFs) may appear: the middle atomic layer changes to the third position with respect to the adjacent

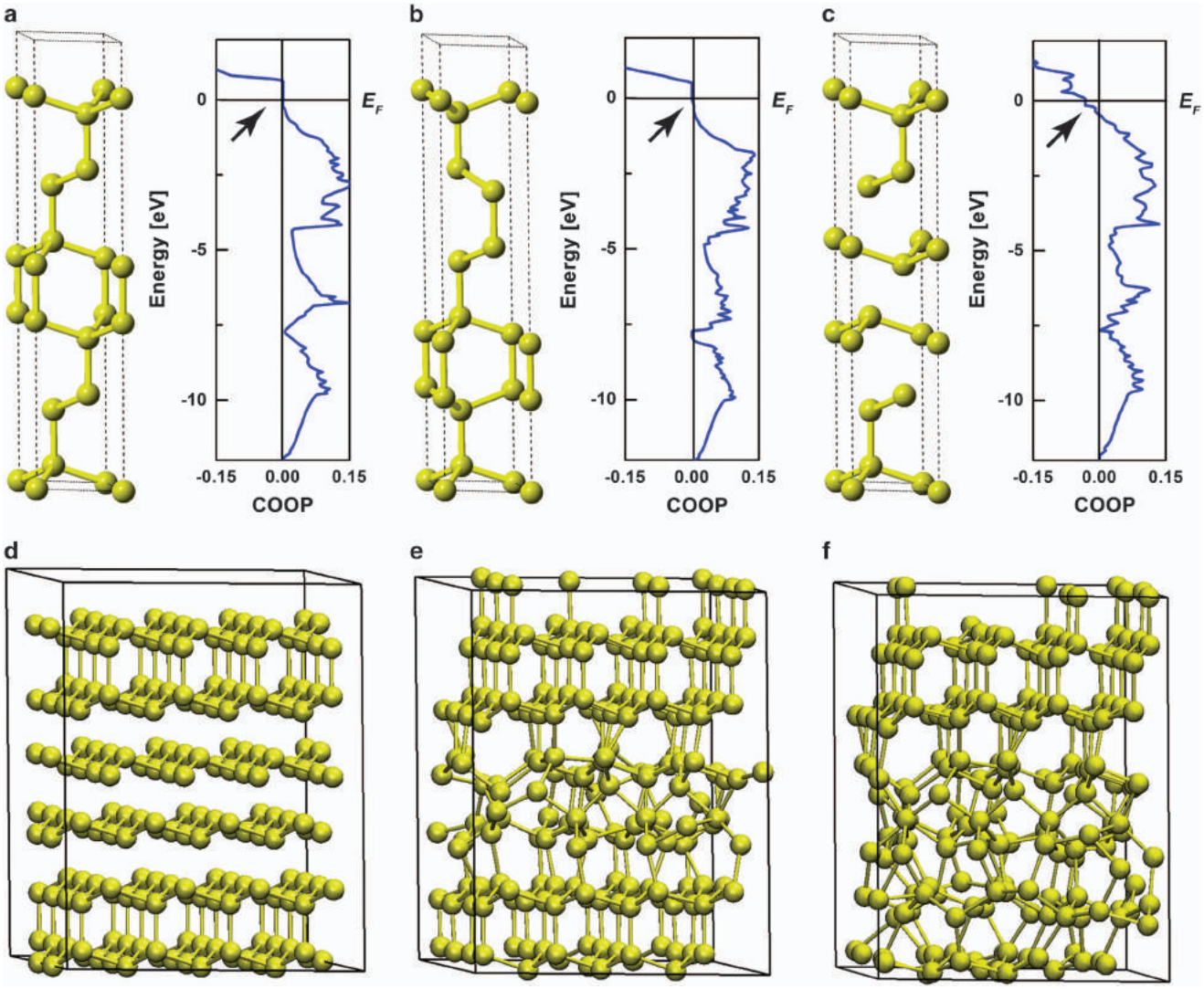

Figure 4 DFT simulations of stacking faults, and the stacking faults induced amorphization. Diamond cubic silicon structure is built along its [111] direction. (**a**) the perfect stacking sequence -AABBCCAABBCC-, (**b**) the sequence with pairwise stacking faults -AABBAABBCCBB- and (**c**) the sequence with single-layer stacking faults -AABBCABCABCC-. The corresponding crystal orbital overlap population (COOP) of the unrelaxed models is shown next to each atomic model (blue curve). The black arrow indicates the bonding configuration near the Fermi level of each model. (**d**) A 4×4 supercell model of that shown in (**c**). (**e**) Upon atomic relaxation at 0 K, the stacking faults region becomes significantly disordered. (**f**) Two more single-layer stacking faults near the disordered region were created manually and the model was relaxed again. The resulting structure is partially amorphized.

two layers, for example, from AAB to ACB. In Figure 4c, we present a model with a sequence -AABBCABCABCC-. In this case, the energy hikes markedly to ~300 meV/atom, and the bonding situation changes substantially, that is, strong antibonding interaction appears near E_F (indicated by the black arrow), suggesting that the system is now unstable and needs to reconfigure its geometry. Then we created a 4×4 supercell (Figure 4d) based on this model and relaxed the whole structure. Clearly, the region with SSFs turns disordered, see Figure 4e, which reduces the energy down to ~140 meV per atom. Apparently, the defect-ridden state is high in energy, but fails to return to the c-Si state due to kinetic limitations. Instead, it falls into an amorphous basin on the complex energy landscape. If there is only one SSF locally, the system could go back to the original Si upon structural relaxation. By loading two more SSFs in the obtained geometry, the system gets further disordered upon atomic relaxation, as shown in Figure 4f. The dynamic process is shown in Supplementary Movie 2. With such a sequential storage of SFs, the crystal is increasingly destabilized and eventually collapses into a fully amorphous phase. The DFT simulations thus depict a very plausible path for the CAT observed in our experiments.

DISCUSSION

To further solidify our understanding of the deformation-induced CAT, we cross-checked our results with respect to two important factors, that is, effects from electron-beam irradiation and unloading strain rate. After imaging the positions of the sample and the flat diamond loading punch in the TEM, the e-beam was blocked off with the condenser lens aperture. The subsequently compressed pillar gave similar CAT configurations as those observed under e-beam, see Supplementary Figure S8. This suggests that the intensity and the exposure time of electron beam used in our TEM experiments would not have a role in the observed CAT. We also performed several additional compression measurements employing different unloading strain rate, ranging from 10^{-3} s^{-1} to 10^{-1} s^{-1}. The results showed

that the CAT process is independent of unloading rate, which differs from those reported in indention experiments,[11,12] suggesting a more controllable way to produce a-Si.

Our observation is different from that found in high-pressure experiments on c-Si,[36–38] where Si-I transforms to Si-II, or to many other crystalline forms, rather than to amorphous phase under high hydrostatic pressure. The absence of a-Si there indicates that plastic deformation is a more effective route to CAT in Si. In our core/shell sample, the stress is such that the von Mises stress (~8.5 GPa) is much bigger than the hydrostatic pressure (~3 GPa). In this case, c-Si is prone to shear plastic strain rather than the volumetric strain during deformation.[10] The high von Mises stress then triggers the profuse formation of SFs along the {111} glide planes, the accumulation of pairwise stacking faults and possible appearance of very unfavorable SSFs in the confined volume, and eventually leads to amorphization. Note that the a-Si/c-Si interface (amorphous–crystalline interface, see Supplementary Figure S7 for its detailed structure) may lower the energy cost for SF formation, but it is not a prerequisite for CAT. This is supported by the HRTEM images showing that the amorphous pockets are often uncorrelated (Figure 3), and some amorphous domains emerge in the interior of pure c-Si regions. In addition, from our DFT simulations, CAT can occur in the absence of amorphous–crystalline interface (Figure 4). We also note that the deformation-induced a-Si is obtained from directional SFs and hence exhibit visible texture-like stripes. The 'trailing' feature in the corresponding fast Fourier transform (Figure 3f) indicates that although the atomic structure is randomized in one direction, a periodic modulation of atomic density persists in the [111] direction, which is quite different from the uniform a-Si (Supplementary Figure S1).

The CAT mechanism revealed here should not be limited to nanoscale objects, but can take place in bulk Si locally, if similar defect accumulation occurs in a constrained volume, leading to strong antibonding interactions and collapse into the amorphous phase. This is partially confirmed in a very recent paper by Zhao *et al.*,[21] in which defect accumulation induced amorphization was observed locally in bulk c-Si under dynamic shock compression, resulting in a complex distribution of a-Si.

It is worth mentioning that such process has also long been believed to be due to the gradual accumulation of defects that elevates the energy of the crystal to above that of the amorphous state in metallic alloys.[39,40] Our current study provides direct evidence of this mechanism, through *in situ* observation of the CAT process from its beginning (pristine crystal) all the way to the end (collapse into the amorphous phase).

CONCLUDING REMARKS

In summary, we have designed a novel and effective c-Si/a-Si core/shell sample configuration, which enabled a real-time and real-space observation of the deformation induced CAT process. The malleable a-Si shell helped to inhibit brittle fracture, and provided the confinement to significantly raise the stress level and extend the plastic flow in the c-Si core. Our *in situ* TEM compression experiment unambiguously demonstrated a direct amorphization process from the single crystalline diamond cubic Si phase. No other intermediate crystalline phases were observed. This, together with the DFT simulations, settles the question as to how and why CAT develops in c-Si upon extensive plastic deformation. Our experimental protocol also opens up the possibility for *in situ* investigation of plastic deformation and deformation-induced amorphization in other brittle solids.

CONFLICT OF INTEREST

The authors declare no conflict of interest.

ACKNOWLEDGEMENTS

This work was supported by grants from National Natural Science Foundation of China (51231005, 51321003 and 11132006). WZ gratefully thanks the Young Talent Support Plan of Xi'an Jiaotong University. WZ acknowledges the computational resources provided by the HPCC platform of Xi'an Jiaotong University. We would like to thank Drs Liang Wan, Lin Tian and Boyu Liu, professor Weizhong Han at Xi'an Jiaotong University, Dr Volker Deringer at University of Cambridge and Dr Jianyu Huang for valuable discussions. We also thank Danli Zhang for assistance in the NanoMill experiments.

1 Deb, S. K., Wilding, M., Somayazulu, M. & McMillan, P. F. Pressure-induced amorphization and an amorphous-amorphous transition in densified porous silicon. *Nature* **414**, 528–530 (2001).
2 Minowa, K. & Sumino, K. Stress-induced amorphization of silicon crystal by mechanical scratching. *Phys. Rev. Lett.* **69**, 320–322 (1992).
3 Takeda, S. & Yamasaki, J. Amorphization in silicon by electron irradiation. *Phys. Rev. Lett.* **83**, 320–323 (1999).
4 Dai, S., Zhao, J., Xie, L., Cai, Y., Wang, N. & Zhu, J. Electron-beam-induced elastic-plastic transition in Si nanowires. *Nano Lett.* **12**, 2379–2385 (2012).
5 Pelaz, L., Marqués, L. A. & Barbolla, J. Ion-beam-induced amorphization and recrystallization in silicon. *J. Appl. Phys.* **96**, 5947 (2004).
6 Clarke, D. R., Kroll, M. C., Kirchner, P. D., Cook, R. F. & Hockey, B. J. Amorphization and conductivity of silicon and germanium induced by indentation. *Phys. Rev. Lett.* **60**, 2156–2159 (1988).
7 Wu, Y. Q., Huang, H., Zou, J., Zhang, L. C. & Dell, J. M. Nanoscratch-induced phase transformation of monocrystalline Si. *Scripta Mater.* **63**, 847–850 (2010).
8 Zarudi, I. & Zhang, L. Effect of ultraprecision grinding on the microstructural change in silicon monocrystals. *J. Mater. Proc. Tech.* **84**, 149–158 (1998).
9 Zhang, L. & Zarudi, I. Towards a deeper understanding of plastic deformation in mono-crystalline silicon. *Int. J. Mech. Sci.* **43**, 1985–1996 (2001).
10 Chrobak, D., Tymiak, N., Beaber, A., Ugurlu, O., Gerberich, W. W. & Nowak, R. Deconfinement leads to changes in the nanoscale plasticity of silicon. *Nat. Nanotechnol.* **6**, 480–484 (2011).
11 Domnich, V., Gogotsi, Y. & Dub, S. Effect of phase transformations on the shape of the unloading curve in the nanoindentation of silicon. *Appl. Phys. Lett.* **76**, 2214 (2000).
12 Ge, D., Minor, A. M., Stach, E. A. & Morris, J. W. Size effects in the nanoindentation of silicon at ambient temperature. *Phil. Mag.* **86**, 4069–4080 (2006).
13 Wu, Y. & Xu, Y. Lattice-distortion-induced amorphization in indented [110] silicon. *J. Mater. Res.* **14**, 682–687 (1999).
14 Suprijadi, M. T., Arai, S. & Saka, H. On the dislocation mechanism of amorphization of Si by indentation. *Phil. Mag. Lett.* **82**, 133–139 (2002).
15 Zhang, L. & Basak, A. Quantitative prediction of phase transformations in silicon during nanoindentation. *Phil. Mag. Lett.* **93**, 448–456 (2013).
16 Gaffet, E. & Harmelin, M. Crystal-amorphous phase transition induced by ball-milling in silicon. *J. Less Common Metals* **157**, 201–222 (1990).
17 Huang, J. Y., Yasuda, H. & Mori, H. Deformation-induced amorphization in ball-milled silicon. *Phil. Mag. Lett.* **79**, 305–314 (1999).
18 Wang, L., Zheng, K., Zhang, Z. & Han, X. Direct atomic-scale imaging about the mechanisms of ultralarge bent straining in Si nanowires. *Nano Lett.* **11**, 2382–2385 (2011).
19 Tang, D. M., Ren, C. L., Wang, M. S., Wei, X., Kawamoto, N., Liu, C., Bando, Y., Mitome, M., Fukata, N. & Golberg, D. Mechanical properties of Si nanowires as revealed by *in situ* transmission electron microscopy and molecular dynamics simulations. *Nano Lett.* **12**, 1898–1904 (2012).
20 Shimomura, O., Minomura, S., Sakai, N., Asaumi, K., Tamura, K., Fukushima, J. & Endo, H. Pressure-induced semiconductor-metal transitions in amorphous Si and Ge. *Phil. Mag.* **29**, 547–558 (1974).
21 Zhao, S., Hahn, E. N., Kad, B., Remington, B. A., Wehrenberg, C. E., Bringa, E. M. & Meyers, M. A. Amorphization and nanocrystallization of silicon under shock compression. *Acta Mater.* **103**, 519–533 (2016).
22 Minor, A. M., Lilleodden, E. T., Jin, M., Stach, E. A., Chrzan, D. C. & Morris, J. W. Room temperature dislocation plasticity in silicon. *Phil. Mag.* **85**, 323–330 (2005).
23 Wang, Y.-C., Xie, D.-G., Ning, X.-H. & Shan, Z.-W. Thermal treatment-induced ductile-to-brittle transition of submicron-sized Si pillars fabricated by focused ion beam. *Appl. Phys. Lett.* **106**, 081905 (2015).
24 Shan, Z., Adesso, G., Cabot, A., Sherburne, M., Asif, S. S., Warren, O., Chrzan, D. C., Minor, A. M. & Alivisatos, A. P. Ultrahigh stress and strain in hierarchically structured hollow nanoparticles. *Nat. Mater.* **7**, 947–952 (2008).

25 Kresse, G. & Furthmüller, J. Efficient iterative schemes for *ab initio* total-energy calculations using a plane-wave basis set. *Phys. Rev. B. Condens. Matter* **54**, 11169–11186 (1996).
26 Perdew, J. P., Burke, K. & Ernzerhof, M. Generalized gradient approximation made simple. *Phys. Rev. Lett.* **77**, 3865–3868 (1996).
27 Blöchl, P. E. Projector augmented-wave method. *Phys. Rev. B* **50**, 17953–17979 (1994).
28 Monkhorst, H. J. & Pack, J. D. Special points for Brillouin-zone integrations. *Phys. Rev. B* **13**, 5188–5192 (1976).
29 Maintz, S., Deringer, V. L., Tchougreeff, A. L. & Dronskowski, R. LOBSTER: a tool to extract chemical bonding from plane-wave based DFT. *J. Comput. Chem.* **37**, 1030–1035 (2016).
30 Tran, F. & Blaha, P. Accurate band gaps of semiconductors and insulators with a semilocal exchange-correlation potential. *Phys. Rev. Lett.* **102**, 226401 (2009).
31 Wang, C.-Z., Li, J., Ho, K.-M. & Yip, S. Undissociated screw dislocation in Si: glide or shuffle set? *Appl. Phys. Lett.* **89**, 051910 (2006).
32 Kushima, A., Liu, X. H., Zhu, G., Wang, Z. L., Huang, J. Y. & Li, J. Leapfrog cracking and nanoamorphization of ZnO nanowires during *in situ* electrochemical lithiation. *Nano Lett.* **11**, 4535–4541 (2011).
33 Chou, M. Y., Cohen, M. L. & Louie, S. G. Theoretical study of stacking faults in silicon. *Phys. Rev. B* **32**, 7979–7987 (1985).
34 Kaxiras, E. & Duesbery, M. S. Free energies of generalized stacking faults in Si and implications for the brittle-ductile transition. *Phys. Rev. Lett.* **70**, 3752–3755 (1993).
35 Hughbanks, T. & Hoffmann, R. Chains of trans-edge-sharing molybdenum octahedra: metal-metal bonding in extended systems. *J. Am. Chem. Soc.* **105**, 3528–3537 (1983).
36 Jamieson, J. C. Crystal structures at high pressures of metallic modifications of silicon and germanium. *Science* **139**, 762–764 (1963).
37 Hu, J. Z., Merkle, L. D., Menoni, C. S. & Spain, I. L. Crystal data for high-pressure phases of silicon. *Phys. Rev. B* **34**, 4679–4684 (1986).
38 Mujica, A., Rubio, A., Munoz, A. & Needs, R. J. High-pressure phases of group-IV, III-V, and II-VI compounds. *Rev. Mod. Phys.* **75**, 863 (2003).
39 Ma, E. Amorphization and metastable polymorphs of ordered intermetallics Z^ Al and N13Al. *J. Mater. Res.* **9**, 593 (1994).
40 Ma, E. & Atzmon, M. Phase transformations induced by mechanical alloying in binary systems. *Mater. Chem. Phys.* **39**, 249–267 (1995).

Supplementary Information accompanies the paper on the NPG Asia Materials website (http://www.nature.com/am)